Journal of Computational Physics 321 (2016) 965–980

Contents lists available at ScienceDirect

Journal of Computational Physics

www.elsevier.com/locate/jcp

A 3D immersed finite element method with non-homogeneous interface flux jump for applications in particle-in-cell simulations of plasma–lunar surface interactions ☆

Daoru Han [a], Pu Wang [b], Xiaoming He [c,*], Tao Lin [d], Joseph Wang [a]

[a] Department of Astronautical Engineering, University of Southern California, Los Angles, CA 90089, USA
[b] Department of Aerospace and Ocean Engineering, Virginia Tech, USA
[c] Department of Mathematics and Statistics, Missouri University of Science and Technology, Rolla, MO 65409, USA
[d] Department of Mathematics, Virginia Tech, Blacksburg, VA 24061, USA

ARTICLE INFO

Article history:
Received 21 September 2015
Received in revised form 23 April 2016
Accepted 27 May 2016
Available online 2 June 2016

Keywords:
Interface problems
Non-homogeneous flux jump conditions
Immersed finite elements
Particle-in-Cell
Plasma environments
Lunar surface

ABSTRACT

Motivated by the need to handle complex boundary conditions efficiently and accurately in particle-in-cell (PIC) simulations, this paper presents a three-dimensional (3D) linear immersed finite element (IFE) method with non-homogeneous flux jump conditions for solving electrostatic field involving complex boundary conditions using structured meshes independent of the interface. This method treats an object boundary as part of the simulation domain and solves the electric field at the boundary as an interface problem. In order to resolve charging on a dielectric surface, a new 3D linear IFE basis function is designed for each interface element to capture the electric field jump on the interface. Numerical experiments are provided to demonstrate the optimal convergence rates in L^2 and H^1 norms of the IFE solution. This new IFE method is integrated into a PIC method for simulations involving charging of a complex dielectric surface in a plasma. A numerical study of plasma–surface interactions at the lunar terminator is presented to demonstrate the applicability of the new method.

1. Introduction

The Particle-in-Cell (PIC) method is a standard tool to model the interactions of a rarefied plasma with complex surfaces of different types of objects. In PIC simulations of plasma–object interaction, the objects' surfaces divide the domain into two or more sub-domains. In order to take into account the electrical interactions between the objects and plasma, the following three-dimensional interface elliptic equation involving the electric field (**E**) discontinuity across the interface needs to be considered for the electric potential $\phi(X)$ [12,30,68]:

☆ This work is partially supported by NSF grant DMS-1016313, NASA grant NNX11AH21G, and University of Missouri Research Board.
* Corresponding author.
E-mail addresses: daoruhan@usc.edu (D. Han), wangpu@vt.edu (P. Wang), hex@mst.edu (X. He), tlin@math.vt.edu (T. Lin), josephjw@usc.edu (J. Wang).

http://dx.doi.org/10.1016/j.jcp.2016.05.057
0021-9991/

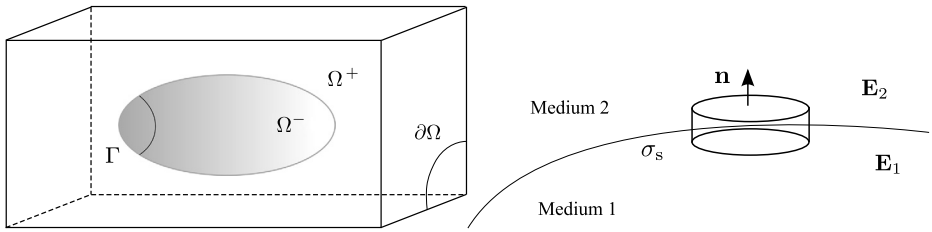

(a) Computation domain including the interface (b) Electric flux jump across the interface

Fig. 1. A sketch of the interface problem.

$$-\nabla\cdot\left(\varepsilon\nabla\phi(X)\right)=\rho(X),\quad X=(x,y,z)\in\Omega^-\cup\Omega^+, \tag{1.1}$$

$$\phi(X)|_{\Gamma_D}=g(X), \tag{1.2}$$

$$\frac{\partial\phi(X)}{\partial\mathbf{n}_{\Gamma_N}}|_{\Gamma_N}=p(X), \tag{1.3}$$

together with the jump conditions across the interface Γ:

$$[\phi(X)]|_\Gamma=0, \tag{1.4}$$

$$\left[\varepsilon\frac{\partial\phi(X)}{\partial\mathbf{n}_\Gamma}\right]\Big|_\Gamma=q(X)=-(\varepsilon_2\mathbf{E_2}-\varepsilon_1\mathbf{E_1})\cdot\mathbf{n}_\Gamma=-\sigma_s. \tag{1.5}$$

Here, see the sketch in Fig. 1, without loss of generality, we assume that $\Omega\subset\mathbb{R}^3$ is a box domain, the interface Γ is a curved surface separating Ω into two sub-domains (Ω^- and Ω^+) such that $\overline{\Omega}=\overline{\Omega^-}\cup\overline{\Omega^+}\cup\Gamma$, Γ_D and Γ_N are the Dirichlet and Neumann boundaries such that $\partial\Omega=\Gamma_D\cup\Gamma_N$, $\mathbf{n}_{\Gamma_N}$ is the unit outer normal vector of Γ_N, $\mathbf{n}_\Gamma$ is the unit normal vector of Γ pointing from Ω^- to Ω^+, E_i $(i=1,2)$ is the electric field in the medium i, and the material-dependent coefficient $\varepsilon(x,y)$ is a piecewise constant function defined by

$$\varepsilon(X)=\begin{cases}\varepsilon^-, & X\in\Omega^-,\\ \varepsilon^+, & X\in\Omega^+.\end{cases}$$

Because PIC simulations spend a significant amount of time on locating a huge number of simulation particles in the mesh at each iteration, it is preferable to utilize structured meshes that can deal with the complex interfaces. However, when conventional numerical methods [3,5,8,28,59] are used to solve the interface problem (1.1)–(1.5), body-fitting meshes, which are unstructured, need to be utilized in order to guarantee these methods' performance. Therefore, the immersed finite element (IFE) methods, which were developed for solving interface problems on meshes independent of interface [1,6,9,15,19,22,23,26,27,31,39–41,43–47,49,50,53,69], have been integrated into the PIC method as the electric field solver on structured meshes. This resulted in the IFE-PIC method [7,11,33,37,51,52,64,68], which has been employed in the modeling of plasma flow in ion thrusters and plume–spacecraft interactions. In these applications, the electric potentials of the objects are assumed to be fixed and known, which yields the homogeneous flux jump condition across the interface for the interface model. Therefore, the existing IFE-PIC method and 3D IFE method [34,58,63] consider only the homogeneous flux jump condition.

This study concerns application problems involving a dielectric object immersed in a plasma. The surface potential on a dielectric surface is determined by local charge deposition, which results in a non-homogeneous flux jump (i.e. electric field) conditions across the interface. In this paper, we develop a three-dimensional immersed finite element method for the second order interface elliptic problems with non-homogeneous flux jump condition, and integrate it to the PIC method. This new IFE-PIC method allows one to solve self-consistently the surface potential of a complex dielectric object and the plasma flow directly from local charge deposition on the surface.

The basic idea of the new IFE method is to locally enrich the 3D linear IFE space in [34] by adding new piecewise polynomials that can approximate the non-homogeneous flux jump conditions satisfactorily [24]. The major difficulty for proposing the new IFE-PIC method lies in the dynamic interaction between the IFE and PIC methods, especially the accumulation of the surface charging q expressed by surface charge density σ_s as shown in Fig. 1b. In addition to the traditional advantages of the IFE and PIC methods, another practical advantage of this new method is the convenience to implement it based on the existing 3D IFE-PIC package for homogeneous interface conditions since the new method keeps the basic framework of the existing IFE space and the method developed in [34].

This new IFE-PIC method is applied to study plasma–surface interactions at the lunar terminator. Without a global magnetic field, the lunar surface is directly exposed to the solar radiation and the space plasma environments. Substantial studies have been carried out to understand the near surface plasma environment on the Moon [14,16,55–57,66–68]. The lunar polar region is of particular interest to future lunar exploration missions due to the availability of solar power and the existence of cold-trapped lunar water/ice. Modeling plasma–surface interactions in the terminator region is a challenging numerical problem as it requires the model to calculate the charging of a complex shaped surface terrain self-consistently

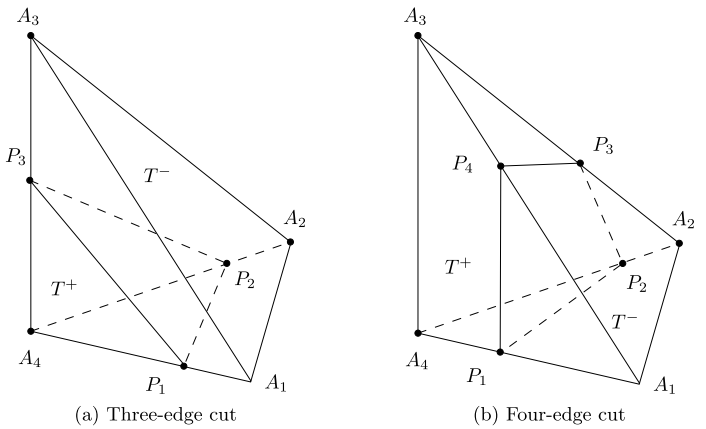

Fig. 2. Intersection topologies for tetrahedral elements.

with the plasma flow field. Previously, finite-difference based PIC models combining plasma simulation with the calculation of the electric field or charging at the boundary surface have been developed (for example, see [62,66,67] and references therein). All published modeling studies on plasma interactions with the lunar surface utilize finite-difference based PIC models which limit their applications to relatively simple surface configurations.

The rest of this article is organized as follows. In Section 2, we construct a 3D linear IFE space for the non-homogeneous flux jump conditions and discuss its approximation capability by using the finite element interpolation with a numerical example. In Section 3 we show how this new IFE space can be used in a Galerkin formulation to solve interface problems with a non-homogeneous flux jump, and a numerical example is presented to show the optimal convergence of the IFE method. In Section 4, the IFE method will be assembled into a PIC method, which is improved for accumulating the surface charge density, in order to form the new IFE-PIC method with non-homogeneous flux jump conditions. A 3D test case is also presented for validation. In Section 5, the new IFE-PIC method will be utilized to simulate the plasma environment on a local uneven surface terrain at the lunar terminator regions. Brief conclusions will be given in Section 6.

2. 3D linear IFE space for the non-homogeneous flux jump condition

In this section we construct and study a three-dimensional linear IFE space that can be used to approximate functions satisfying the interface conditions (1.4) and (1.5). We first recall the 3D local linear IFE space capable of handling the corresponding homogeneous jump condition $[\varepsilon \frac{\partial \phi(X)}{\partial \mathbf{n}_\Gamma}]|_\Gamma = 0$ from [34]. Then we describe how to enrich this space locally in each interface element by adding a new IFE function that is constructed based on the non-homogeneous flux jump condition (1.5). The computation of the coefficients of the new IFE function will be discussed shortly. Finally, we define the corresponding global IFE space for the non-homogeneous jump condition and investigate on its approximation capability by utilizing the IFE interpolation with a numerical experiment.

First, we introduce a typical tetrahedron mesh $\mathcal{T}_h$ on Ω that is independent of the interface Γ. When the mesh size is small enough, only a small portion of elements in $\mathcal{T}_h$ are cut through by the interface Γ and we call them the interface elements. Most of the elements are non-interface elements. Without loss of generality, we only consider the following two typical intersection topologies (see Fig. 2) when the mesh size is small enough [34]:

1. Three-edge cut: The interface surface Γ intersects with the edges of an element T at three distinct points which are not on the same face of T.
2. Four-edge cut: The interface surface Γ intersect with the edges of an element T at four distinct points on four different edges, and each three of these intersection points are not on a line.

On a typical non-interface tetrahedron element T with vertices $A_i (i = 1, 2, 3, 4)$, we can use the usual local 3D linear finite element space $S_h(T) = span\{\psi_i(x, y), i = 1, 2, 3, 4\}$ with 3D linear polynomials such that

$$\psi_i(A_j) = \begin{cases} 1, & \text{if } i = j \\ 0, & \text{if } i \neq j. \end{cases} \tag{2.6}$$

On the other hand, for each interface tetrahedron element T, we can use the 3D IFE functions developed in [34]. To describe these IFE functions on a typical interface element T, we use the strategy in [34] to select three points P_1, P_2, P_3 on the intersection of the interface and T. Assume the intersection between the plane determined by these three points and T is $\overline{\Gamma}_T$, which separates T into two sub-elements T^- and T^+, as shown in Fig. 3 (see [34] for more details). Then the IFE functions introduced in [34] are characterized by the following formula:

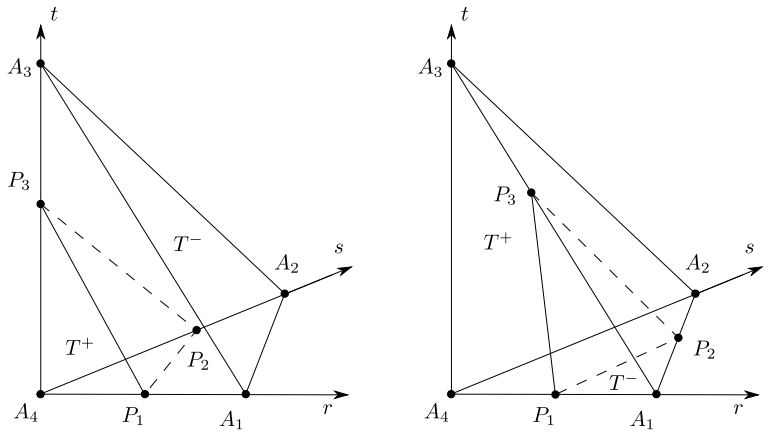

Fig. 3. Two cases of possible three-edge cut in the reference element $\hat{T}$.

$$\varphi(x,y,z)=\begin{cases}\varphi^-(x,y,z)=a^-x+b^-y+c^-z+d^-, & (x,y,z)\in T^-,\\ \varphi^+(x,y,z)=a^+x+b^+y+c^+z+d^+, & (x,y,z)\in T^+,\\ \varphi^-(P_1)=\varphi^+(P_1),\ \ \varphi^-(P_2)=\varphi^+(P_2),\ \ \varphi^-(P_3)=\varphi^+(P_3),\\ \varepsilon^+\dfrac{\partial\varphi^+}{\partial\mathbf{n}}-\varepsilon^-\dfrac{\partial\varphi^-}{\partial\mathbf{n}}=0, & \text{on } \overline{\Gamma}_T\end{cases}\tag{2.7}$$

where $\mathbf{n}=(n_1,n_2,n_3)$ is the unit normal vector of $\overline{\Gamma}_T$ pointing from T^- to T^+. It has been shown in [34] that, for each $i=1,2,3,4$, there exists a unique IFE function $\varphi_i(x,y,z)$ such that

$$\varphi_i(A_j)=\begin{cases}1, & \text{if } i=j,\\ 0, & \text{if } i\neq j.\end{cases}\tag{2.8}$$

Then the local 3D linear immersed finite element space is defined as $S_h(T)=span\{\varphi_i(x,y,z), i=1,2,3,4\}$ in [34], which can only handle the homogeneous flux jump conditions.

Furthermore, in order to handle the non-homogeneous flux jump conditions on an interface element T, we follow the idea in [24] to design the following 3D IFE function $\varphi_{T,J}(x,y,z)$ which is zero at all the vertices of T but has a unit flux jump.

$$\varphi_{T,J}(x,y,z)=\begin{cases}\varphi^-_{T,J}(x,y,z)=a^-_Jx+b^-_Jy+c^-_Jz+d^-_J, & (x,y,z)\in T^-,\\ \varphi^+_{T,J}(x,y,z)=a^+_Jx+b^+_Jy+c^+_Jz+d^+_J, & (x,y,z)\in T^+,\\ \varphi^-_{T,J}(P_1)=\varphi^+_{T,J}(P_1),\ \varphi^-_{T,J}(P_2)=\varphi^+_{T,J}(P_2),\ \varphi^-_{T,J}(P_3)=\varphi^+_{T,J}(P_3),\\ \varepsilon^+\dfrac{\partial\varphi^+_{T,J}}{\partial\mathbf{n}}-\varepsilon^-\dfrac{\partial\varphi^-_{T,J}}{\partial\mathbf{n}}=1, & \text{on } \overline{\Gamma}_T\\ \varphi_{T,J}(A_j)=0, & j=1,2,3,4.\end{cases}\tag{2.9}$$

Then the new local 3D IFE space on the interface element can be defined as:

$$S_h^J(T)=span\{\varphi_{T,J}(x,y,z),\varphi_i(x,y,z):i=1,2,3,4\}.\tag{2.10}$$

To shortly describe the computation of the coefficients in $\varphi_{T,J}(x,y,z)$, we consider the reference element $\hat{T}$ with vertices $\hat{A}_i$ $(i=1,2,3,4)$ where $\hat{A}_1=(1,0,0)$, $\hat{A}_2=(0,1,0)$, $\hat{A}_3=(0,0,1)$, and $\hat{A}_4=(0,0,0)$. Consider the intersection case shown in the left panel of Fig. 3, assume the coordinates of the three points P_1, P_2, P_3 are:

$$P_1=[\xi,0,0]^T,\ P_2=[0,\eta,0]^T,\ P_3=[0,0,\zeta]^T,\tag{2.11}$$

where $0\le\xi\le1$, $0\le\eta\le1$, $0\le\zeta\le1$. Let $\hat{\mathbf{n}}=(\hat{n}_1,\hat{n}_2,\hat{n}_3)$ denote the unit normal vector of $\triangle P_1P_2P_3$ pointing from $\hat{T}^-$ to $\hat{T}^+$. Then, the eight equations arising from (2.9) are:

$$d^+_J=\varphi_{T,J}(A_4)=0\tag{2.12}$$

$$a^-_J+d^-_J=\varphi_{T,J}(A_1)=0\tag{2.13}$$

$$b^-_J+d^-_J=\varphi_{T,J}(A_2)=0\tag{2.14}$$

$$c^-_J+d^-_J=\varphi_{T,J}(A_3)=0\tag{2.15}$$

$$\xi a^+_J+d^+_J=\varphi^+_{T,J}(P_1)=\varphi^-_{T,J}(P_1)=\xi a^-_J+d^-_J\tag{2.16}$$

$$\eta b_J^+ + d_J^+ = \varphi_{T,J}^+(P_2) = \varphi_{T,J}^-(P_2) = \eta b_J^- + d_J^- \tag{2.17}$$

$$\zeta c_J^+ + d_J^+ = \varphi_{T,J}^+(P_3) = \varphi_{T,J}^-(P_3) = \zeta c_J^- + d_J^- \tag{2.18}$$

$$\varepsilon^+(\hat{n}_1 a_J^+ + \hat{n}_2 b_J^+ + \hat{n}_3 c_J^+) - \varepsilon^-(\hat{n}_1 a_J^- + \hat{n}_2 b_J^- + \hat{n}_3 c_J^-) = 1. \tag{2.19}$$

Solving these equations, we obtain the following unique set of coefficients, which guarantees the existence and uniqueness of the basis function $\varphi_{T,J}$:

$$a_J^+ = \frac{1-\xi}{\xi} d_J^-,\ \ b_J^+ = \frac{1-\eta}{\eta} d_J^-,\ \ c_J^+ = \frac{1-\zeta}{\zeta} d_J^-,\ \ d_J^+ = 0, \tag{2.20}$$

$$a_J^- = -d_J^-,\ \ b_J^- = -d_J^-,\ \ c_J^- = -d_J^-,\ \ d_J^- = \frac{\lambda_1}{\varepsilon^+\lambda_2 + \varepsilon^-\lambda_3}, \tag{2.21}$$

where

$$\lambda_1 = \xi\eta\zeta,\ \ \lambda_2 = \hat{n}_1(1-\xi)\eta\zeta + \hat{n}_2(1-\eta)\xi\zeta + \hat{n}_3(1-\zeta)\xi\eta,\ \ \lambda_3 = (\hat{n}_1 + \hat{n}_2 + \hat{n}_3)\xi\eta\zeta.$$

Now we use the new local IFE space $S_h^J(T)$ to define a new global 3D linear IFE space $S_h^J(\Omega)$. Suppose there are N nodes and M interface elements in $\mathcal{T}_h$. Then, we define a piecewise 3D linear global nodal basis function $\Psi_j(x,y,z)$ $(j = 1,\cdots,N)$ for each node $(x_j, y_j, z_j)^t$ of $\mathcal{T}_h$ such that $\Psi_j(x_j, y_j, z_j) = 1$ but Ψ_j is zero at other nodes, $\Psi_j|_T \in S_h^J(T)$ with a zero flux jump for any interface element $T \in \mathcal{T}_h$, and $\Psi_j|_T \in S_h(T)$ for any non-interface element $T \in \mathcal{T}_h$. Additionally, we define a piecewise 3D linear global nodal basis function $\Psi_{Jk}(x,y)$ $(k = 1,\cdots,M)$ for the kth interface element T_k of $\mathcal{T}_h$ such that $\Psi_{Jk}|_{T_k} = \phi_{T_k,J}$ and Ψ_{Jk} is zero everywhere else. Finally, we define $S_h^J(\Omega) = span\{\Psi_j(x,y,z), \Psi_{Jk}(x,y,z) : j = 1,\cdots,N;\ k = 1,\cdots,M\}$.

In the following, we will define the finite element interpolation in the new 3D linear IFE space $S_h^J(\Omega)$ and utilize it to investigate the approximation capability of the space $S_h^J(\Omega)$ for continuous functions that have a non-homogeneous flux jump across the interface.

For any subset $\Lambda \subset \Omega$ whose interior is cut through by the interface Γ, we define

$$PH_{int}^2(\Lambda) = \left\{ \phi \in C(\Lambda), \phi|_{\Lambda^s} \in H^2(\Lambda^s), s = -,+, \left[\varepsilon \frac{\partial \phi}{\partial \mathbf{n}_\Gamma}\right] = q \ \text{ on } \Gamma \cap \Lambda \right\}.$$

For a given function $\phi \in PH_{int}^2(\Lambda)$, we first construct the local IFE interpolation on each element T in a mesh $\mathcal{T}_h$ as follows. If T is a non-interface element, we define the interpolation of ϕ on T by

$$I_{h,T}\phi(X) = \sum_{i=1}^{4} \phi(A_i)\psi_i(X)$$

for $X = (x,y,z) \in T$. On an interface element $T \in \mathcal{T}_h$, we define the IFE interpolation of ϕ by

$$I_{h,T}\phi(X) = \sum_{i=1}^{N_T} \phi(A_i)\varphi_i(X) + q_T\varphi_{T,J}(X),$$

where

$$q_T = \frac{1}{|\bar{\Gamma}_T|} \int_{\bar{\Gamma}_T} q dS. \tag{2.22}$$

Then the global IFE interpolation for a function $\phi \in PH_{int}^2(\Omega)$ can be defined as $I_h\phi \in S_H^J(\Omega)$ such that $I_h\phi|_T = I_{h,T}(\phi|_T)$ for any $T \in \mathcal{T}_h$. Using the properties of the local IFE functions, we can show that the IFE function $I_h\phi$ on an interface element T has the following features:

- $I_{h,T}\phi(A_i) = \phi(A_i)$ $(i = 1,2,3,4)$ and this implies $I_{h,T}\phi(X)$ interpolates $\phi(X)$ on T.
- $\left[I_{h,T}\phi\right]_{\bar{\Gamma}_T} = 0$ which implies that $I_{h,T}\phi \in C^0(T)$ and $I_{h,T}\phi$ locally satisfies the interface condition (1.4).

All of these properties suggest that $I_h\phi$ should be a reasonable approximation to ϕ. The existing analysis works for different IFE spaces show that they have the optimal accuracy orders for the interpolation errors and hence the optimal approximation capability [2,20,21,42]. Here we use the following numerical example to demonstrate that $I_h\phi$ can approximate ϕ with an optimal convergence rate provided that ϕ has enough piecewise smoothness.

Consider $\Omega = (-1,1) \times (-1,1) \times (-1,1)$. The interface Γ is a sphere centered at the origin $(0,0,0)$ with radius $r_0 = 0.4051$, which separates the domain into two subdomains Ω^- and Ω^+ with $\Omega^- = \{(x,y,z) : x^2 + y^2 + z^2 \le r_0^2\}$.

Table 1
Errors in the 3D linear IFE interpolation $I_h u$.

h	$\|I_h u - u\|_0$	$\|I_h u - u\|_1$
1/20	0.00719936258	0.3061815025
1/25	0.00460761352	0.2449285280
1/32	0.00281226556	0.1913444061
1/40	0.00179986496	0.1530734428
1/50	0.00115190276	0.1224568242
1/64	0.00070306438	0.0956674239
1/80	0.00044996093	0.0765335987
1/100	0.00028797420	0.0612264756

The approximated function and coefficient ε are chosen to be

$$\phi(x, y, z) = (x^2 + y^2 + z^2)^{3/2} \tag{2.23}$$

and

$$\varepsilon(x, y) = \begin{cases} \varepsilon^- = 2, & (x, y, z) \in \Omega^-, \\ \varepsilon^+ = 1, & (x, y, z) \in \Omega^+, \end{cases}$$

respectively. Note that $\phi(x, y, z)$ satisfies the following jump conditions:

$$[\phi]_\Gamma = 0, \quad \left[\varepsilon \frac{\partial \phi(X)}{\partial \mathbf{n}_\Gamma}\right]\Big|_\Gamma = 3(\varepsilon^+ - \varepsilon^-)(x^2 + y^2 + z^2).$$

Hence the flux jump is

$$q(x, y, z) = 3(\varepsilon^+ - \varepsilon^-)(x^2 + y^2 + z^2). \tag{2.24}$$

The errors of $I_h\phi$ in the L^2 and semi-H^1 norms are listed in Table 1. To generate data in this table, we use a Cartesian mesh $\mathcal{T}_h$ for each h that is formed by partitioning Ω with boxes of size $h \times h \times h$, and then dividing each box into five tetrahedrons along the diagonal lines. Using the linear regression, we can see that the data in this table obey

$$\|I_h\phi - \phi\|_0 \approx 2.8798\, h^{2.0000}, \quad |I_h\phi - \phi|_1 \approx 6.1250\, h^{1.0001}$$

which indicate that $I_h\phi$ can approximate ϕ optimally in both L^2 norm and semi-H^1 norm.

3. 3D linear IFE method for a model interface problem with non-homogeneous flux jump

In this section, we will introduce and numerically validate a Galerkin method with the new 3D IFE space $S_h^J(\Omega)$ to solve a model interface problem with non-homogeneous flux jump condition.

First, we have the weak formulation for the model interface problem: find $\phi \in H^1(\Omega)$ such that

$$\int_\Omega \varepsilon \nabla\phi \cdot \nabla v \, dxdy = \int_\Omega \rho v \, dxdy + \int_{\Gamma_N} pv ds - \int_\Gamma qv ds, \forall\, v \in H^1_{0D}, \tag{3.25}$$

where $H^1_{0D}(\Omega) = \{v \in H^1(\Omega) : v = 0 \text{ on } \Gamma_D\}$.

Based on a mesh $\mathcal{T}_h$ of the solution domain Ω, we define

$$\mathcal{N}_h = \{(x_i, y_i, z_i)^t \in \mathbb{R}^3 \mid (x_i, y_i, z_i)^t \text{ is a node of } \mathcal{T}_h\},$$
$$\mathcal{N}_h^o = \mathcal{N}_h \cap (\Omega \cup \Gamma_N),$$
$$\mathcal{N}_h^b = \mathcal{N}_h \cap \Gamma_D,$$
$$\mathcal{T}_h^i = \{T \in \mathcal{T}_h \mid T \text{ is an interface element}\}.$$

Then, the IFE interpolation discussed in the previous section suggests we look for an IFE solution to the interface problem in the following form:

$$\phi_h(X) = \sum_{(x_j, y_j, z_j) \in \mathcal{N}_h^o} \phi_j \Psi_j(X) + \sum_{(x_j, y_j, z_j) \in \mathcal{N}_h^b} g(X_j)\Psi_j(X) + \sum_{T_k \in \mathcal{T}_h^i} q_T \Psi_{Jk}(X) \tag{3.26}$$

with coefficient ϕ_j to be determined, where $g(X)$ and q_T are given in (1.2) and (2.22) respectively.

Table 2
The errors of the 3D linear IFE solutions for the interface problem.

h	$\|u_h - u\|_0$	$\|u_h - u\|_1$
1/20	0.0055169524	0.2419986152
1/25	0.0035467267	0.1925017621
1/32	0.0021499146	0.1493660743
1/40	0.0013533077	0.1188110521
1/50	0.0008688439	0.0947487154
1/64	0.0005292758	0.0738441154
1/80	0.0003362958	0.0589198287
1/100	0.0002153340	0.0470062393

Finally, using the weak form (3.25), we have the following equations for the IFE solution ϕ_h:

$$\begin{aligned}
&\sum_{(x_j,y_j,z_j)\in\mathcal{N}_h^o}\left(\sum_{T\in\mathcal{T}_h}\int_T \varepsilon\nabla\Psi_i\cdot\nabla\Psi_j dX\right)\phi_j\\
&=\int_\Omega \rho\Psi_i dX+\int_{\Gamma_N} p\Psi_i ds-\int_\Gamma q\Psi_i ds-\sum_{(x_j,y_j,z_j)\in\mathcal{N}_h^b}\left(\sum_{T\in\mathcal{T}_h}\int_T \varepsilon\nabla\Psi_i\cdot\nabla\Psi_j dX\right)g(X_j)\\
&\quad-\sum_{T_k\in\mathcal{T}_h^i} q_T\left(\int_{T_k}\varepsilon\nabla\Psi_i\cdot\nabla\Psi_{Jk}dX\right),\ \forall i \text{ such that } (x_i,y_i,z_i)\in\mathcal{N}_h^o.
\end{aligned}\tag{3.27}$$

The existing IFE methods in the literature have the optimal convergence rates expected from the utilized polynomials and provide symmetric positive definite matrices for fast solvers [10,17,18,25,38,48,70]. Here we present a numerical example to demonstrate the convergence of the new 3D IFE method solving interface problems with the non-homogeneous flux jump condition. In this example, the source term, boundary conditions, and interface conditions are chosen such that the exact solution $\phi(x, y, z)$ of (1.1)–(1.5) is defined by (2.23) and a Dirichlet boundary condition is imposed on the whole $\partial\Omega$. We also use the same domains and parameters as in the example of the previous section.

The errors in the L^2 and semi-H^1 norms for the 3D linear IFE solutions are listed in Table 2 from which we have

$$\|\phi_h-\phi\|_0\approx 2.3399\,h^{2.0187},\quad |\phi_h-\phi|_1\approx 5.0914\,h^{1.0178}.$$

This demonstrates that the IFE method can solve the interface problems with non-homogeneous flux jump conditions with optimal convergence rates.

4. 3D IFE-PIC method with non-homogeneous flux jump conditions

In this section, we first discuss the integration of the non-homogeneous IFE solver for the electric potential into a legacy particle-in-cell (PIC) code which forms a new non-homogeneous IFE-PIC method. Then we provide a validation of the new IFE-PIC method on a 3D setup.

4.1. IFE-PIC method

In a PIC method, real plasma particles are usually represented by a number of simulation particles (also referred to as *macro-particles* or *super-particles*) distributed "freely" in the entire simulation domain, while the field quantities such as electric potential are discretized on a mesh. The quantities carried by the simulation particles are weighted onto the mesh nodes for the solution of the field, which is in turn interpolated at particle positions to update the velocity/position of the particles. Such data exchange between particles and field quantities will iterate for a desired number of steps to obtain the self-consistent solution of both plasma and fields.

For a collisionless, unmagnetized plasma under an electrostatic field, the trajectory of each charged particle is determined by Newton's second law and Lorentz force:

$$\mathbf{F}=q(\mathbf{E}+\mathbf{v}\times\mathbf{B})=m\frac{\mathrm{d}\mathbf{v}}{\mathrm{d}t}\tag{4.28}$$

where $\mathbf{F}$ is the force, q is electric charge carried by each particle and $\mathbf{v}$ is the velocity vector, which is

$$\mathbf{v}=\frac{\mathrm{d}\mathbf{x}}{\mathrm{d}t}\tag{4.29}$$

where $\mathbf{x}$ is the position vector.

Table 3
Normalization reference parameters.

L_{ref}	q_{ref}	m_{ref}	T_{ref}	Φ_{ref}	ϵ_{ref}	n_{ref}	v_{ref}	t_{ref}
λ_D	e	m_e	T_e	kT_e/e	ϵ_0	n_e	$v_{\vec{e}}$	$1/\omega_{pe}$

The electric field **E** is calculated from electric potential ϕ by

$$\mathbf{E} = -\nabla\phi \tag{4.30}$$

where ϕ is determined by the electric potential interface problem (1.1)–(1.3) posed in a domain Ω.

In the study presented here, the external magnetic field **B** is neglected, which is valid for local plasma–surface interactions on the Moon.

In order to reduce round-off errors when calculating too large or too small numerical values, the above governing equations are usually normalized with reference parameters. Those parameters are usually based on electrons in full-PIC simulations where both electrons and ions are represented by simulation particles, since they are much more mobile than ions. Following are the choices of reference parameters in the normalization.

The lengths are normalized by the Debye length, which is calculated as,

$$L_{\text{ref}} = \lambda_D = \sqrt{\frac{\epsilon_0 k T_e}{n_e e^2}} \tag{4.31}$$

where k is Boltzmann constant; T_e is electron temperature; n_e is the electron number density. The reference velocity is chosen to be electron thermal velocity:

$$v_{\text{ref}} = v_{te} = \sqrt{\frac{kT_e}{m_e}} \tag{4.32}$$

where m_e is electron mass. Physical time is normalized based on electron plasma frequency, which is,

$$\frac{1}{t_{\text{ref}}} = \omega_{pe} = \sqrt{\frac{4\pi n_e e^2}{m_e}} \tag{4.33}$$

in the unit of s^{-1}. A full list of the reference parameters are summarized in Table 3.

With the above reference parameters, the dimensional quantities are normalized such as,

$$\hat{X} = \frac{X}{X_{\text{ref}}} \tag{4.34}$$

where $\hat{X}$ denotes the normalized (dimensionless) quantity.

Writing each dimensional quantity in terms of normalized quantity and reference quantity, and plugging back into the dimensional form of the governing equations, one would get the following normalized system for the PIC code package,

$$\hat{\mathbf{F}} = \hat{q}\hat{\mathbf{E}} = \hat{m}\frac{\mathrm{d}\hat{\mathbf{v}}}{\mathrm{d}\hat{t}} \tag{4.35}$$

$$\hat{\mathbf{v}} = \frac{\mathrm{d}\hat{\mathbf{x}}}{\mathrm{d}\hat{t}} \tag{4.36}$$

$$\nabla\cdot(\hat{\epsilon}\nabla\hat{\Phi}) = -\hat{\rho} \tag{4.37}$$

$$\hat{\mathbf{E}} = -\nabla\hat{\Phi} \tag{4.38}$$

which have the same form as the dimensional equations.

A PIC simulation model has the following major steps in order to solve for plasma dynamics and field quantities self-consistently:

- **Charge Weighting:** The charges carried by simulation particles are "scattered" from the particle locations to the mesh nodes with the weights provided by linear interpolation ("first-order" weighting [4]). By accumulating all these scattered charges on all the mesh nodes, the total charge density, which is the right hand side $\rho(X)$ of the elliptic interface equation (1.1), is provided;
- **Solving for Field:** The interface elliptic problem described by (1.1)–(1.5) is solved for electric potential Φ;
- **Force Weighting:** In order to update the velocity of particles by (4.35), the electric field is obtained from the electric potential and then "gathered" from the mesh nodes to the particle positions with the same weights as in the charge weighting step;
- **Moving Particles:** The equation of motion (4.36) is solved to update the position of each simulation particle.

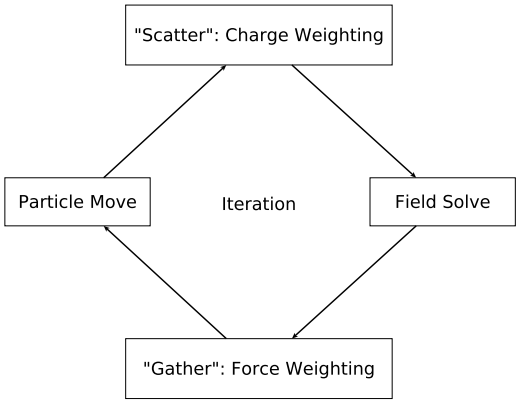

Fig. 4. PIC loop.

The above procedure are iterated (see Fig. 4) for a certain number of simulation steps until a self-consistent solution of both plasma and field is obtained. The charge/force weighting scheme for particles inside non-interface elements is the same as the classic methods in [4] where tri-linear volumes are used as weights. For particles inside interface elements, the charge weighting is still the same, however, the force weighting uses IFE basis functions as the weights in the interpolation of IFE field solution.

As mentioned earlier, the development of the non-homogeneous IFE method presented in this paper is motivated by the need of particle-in-cell simulations of plasma interactions with astronautical applications. For example, 3D IFE-PIC method has been used to model plasma dynamics on ion optics and spacecraft–plume interactions [32–37,64]. However, all the existing works on 3D problems only consider homogeneous flux jump conditions rather than the non-homogeneous ones, which are essential for the modeling of plasma interactions on the lunar surface. This is because the collection of impacting charged particles at the lunar surface combined with photoelectron emissions will lead to surface charging at the top of the lunar regolith, which causes a non-zero flux jump of the electric field across the interface between lunar regolith and space, as described in (1.5) and illustrated in Fig. 1b. Therefore, the non-homogeneous IFE method which is able to handle such non-zero flux jump conditions provides a favorable solver for the PIC method in the modeling of such plasma interactions on the lunar surface. Thus, the new non-homogeneous IFE-PIC method has both capabilities of resolving non-zero electric field flux jump self-consistently with the solution of electric field and handling realistic non-trivial geometries, which is much favorable for the modeling of lunar surface plasma interactions. The detailed non-homogeneous IFE-PIC framework is as follows, also illustrated in Fig. 5:

- Step 1: Construct a Cartesian mesh and obtain the intersection points between the mesh lines and the interface for constructing IFE basis functions;
- Step 2: Initialize velocities and positions of charged particles;
- Step 3: Deposit charges carried by particles onto the mesh nodes in order to obtain the source term $\rho(X)$ in (1.1);
- Step 4: Collect the particles hitting the objects and accumulate their charges on the object surfaces to obtain the non-homogeneous flux jump $q(X)$ in (1.5) for each interface element;
- Step 5: Solve the interface problem (1.1)–(1.5) for the approximated electric field (see $\phi_h(X)$ in (3.26)) self-consistently by using the non-homogeneous IFE method proposed in Section 3;
- Step 6: Interpolate field quantities at particle positions to obtain particle accelerations;
- Step 7: Push particles and apply particle boundary conditions (injection, absorption, reflection, periodic, etc.);
- Step 8: Repeat Step 3–Step 7 until the steady state is reached.

Among the above steps, the accumulation of the charge of the particles hitting the objects onto the object surfaces is a new and necessary step which we need to assemble into the traditional PIC method. In fact, it is the most critical part of the non-homogeneous IFE-PIC method, as it provides the surface charge density for PIC as well as the non-homogeneous flux jump condition for IFE. Here we presents the method of collecting particles and accumulating charges at the interface for a general shape described by a given algebraic equation $z = z(x, y)$ (referred to as "z-surface"), such that the z-surface divides the domain into Ω^+ and Ω^-.

The IFE formulation is constructed following the discussions in Section 2. Within each PIC step, we denote the *old* and *new* positions of a particle as $X_{p_{\text{old}}}$ and $X_{p_{\text{new}}}$, respectively, as shown in Fig. 6. A particle is determined to hit an object under a condition such that

$$z_{p_{\text{old}}} > z(x_{p_{\text{old}}}, y_{p_{\text{old}}}), \quad \text{and} \tag{4.39}$$

$$z_{p_{\text{new}}} < z(x_{p_{\text{new}}}, y_{p_{\text{new}}}). \tag{4.40}$$

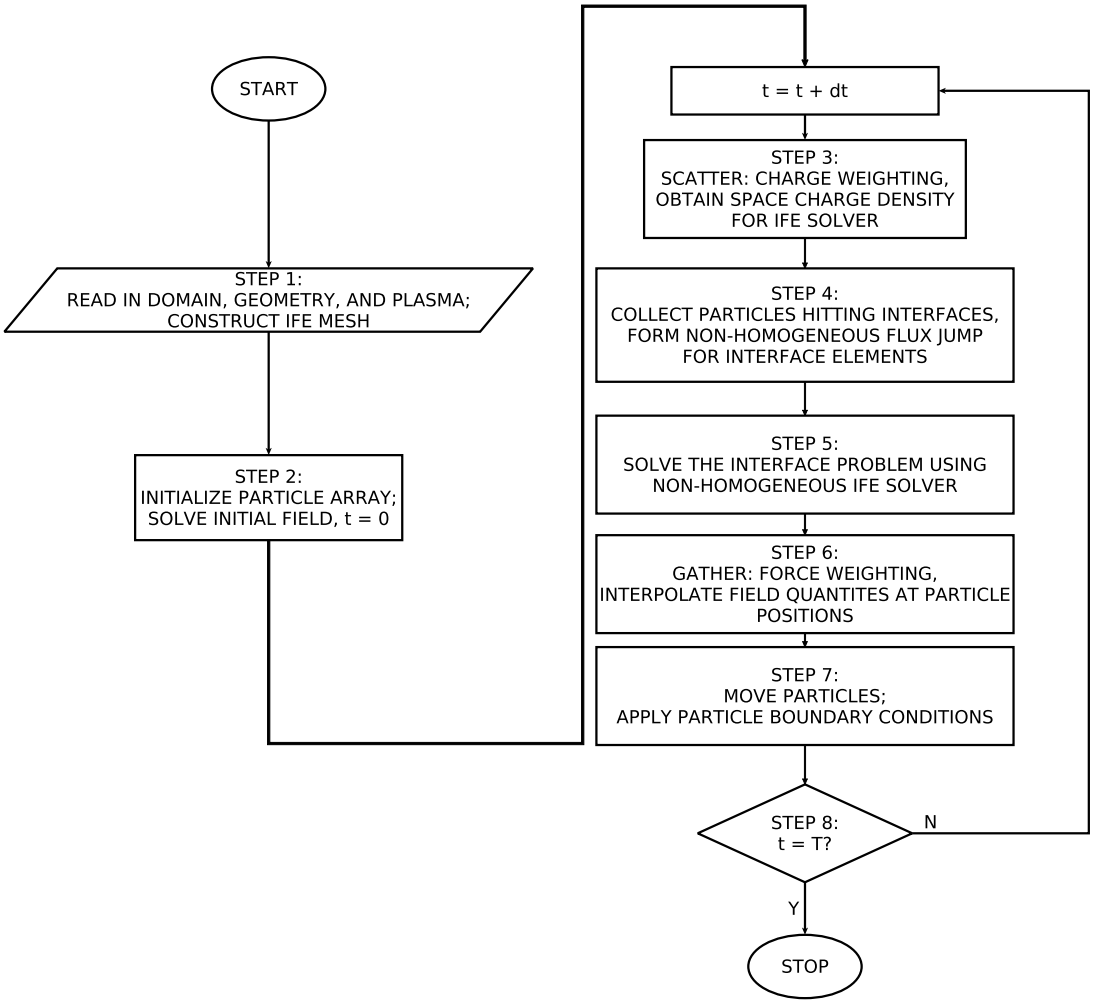

Fig. 5. Flowchart of the IFE-PIC method.

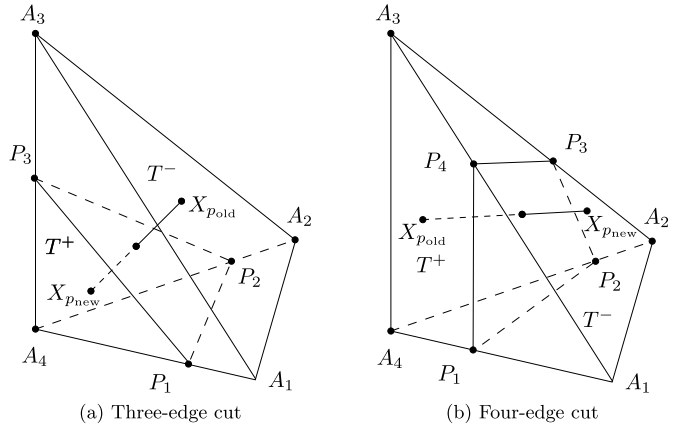

Fig. 6. Particle collection and charge accumulation at interface elements.

Once a particle is determined to hit an object within an interface element T, the charge carried by this particle is added to the total collected charge c_T in this element and this particle is removed from the simulation. Then the q_T, which is defined in (2.22) and needed for the IFE solution in (3.26), can be calculated as follows

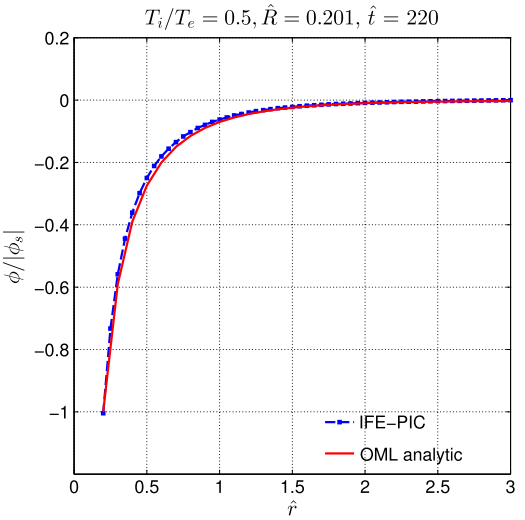

Fig. 7. 1D potential profiles: IFE-PIC vs. OML analytic solution.

$$q_T = \frac{c_T}{A_T} \tag{4.41}$$

where A_T the area of $\overline{\Gamma}_T$ within the interface element.

The resulting surface charge density from such an accumulation step provides the non-zero flux jump condition for the non-homogeneous IFE method, which solves for the electric field self-consistently with plasma kinetics. The solved electric field in turn will govern the motions of charged particles. Such a dynamic interaction between non-homogeneous IFE and PIC about surface charging forms a new simulation tool for modeling the plasma environment on the lunar surface with realistic geometric configurations.

4.2. Validation of the non-homogeneous IFE-PIC method

Before we apply the non-homogeneous IFE-PIC method to the modeling of lunar surface–plasma interactions, we first present a validation test of the method with charging of a dielectric sphere in stationary plasmas. Consider a dielectric sphere in a collisionless, stationary plasma with ion and electron temperature ratio of 0.5 ($T_i = 0.5T_e$). The floating potential at the sphere surface Φ_s is determined by the current balance condition. The ambient ion and electron fluxes are

$$J_i = en_0\sqrt{\frac{kT_i}{2\pi m_i}}\left(1 - \frac{e\Phi_s}{kT_i}\right) \tag{4.42}$$

$$J_e = en_0\sqrt{\frac{kT_e}{2\pi m_e}}\exp\left(\frac{e\Phi_s}{kT_e}\right) \tag{4.43}$$

where n_0 is the ambient plasma density. The analytic formula of ion and electron densities are given by the revised Orbit-Motion-Limited (OML) theory [13,61]. Therefore, the analytic potential profile near the sphere can be obtained numerically by solving Poisson's equation in spherical coordinates. Details of the formulation of the revised OML theory can be found in Refs. [13,61].

In the test, we consider the realistic ion-to-electron mass ratio of $m_i/m_e = 1836$. The floating potential of the sphere is found to be $\Phi_s/T_e = -2.3602$. In the simulation, we use a computation domain of a $3 \times 3 \times 3$ Debye cube with the mesh size of $d = 0.05\lambda_D$ in all dimensions. Therefore, the simulation domain has $60 \times 60 \times 60$ PIC cells. The sphere is centered at $(0, 0, 0)$ with a radius of $R_s = 0.201$. Due to symmetry in all three dimensions, only 1/8 of the sphere is included in the domain. At $X_{\max}$, $Y_{\max}$, $Z_{\max}$ boundaries, the potentials are set to 0. At $X_{\min}$, $Y_{\min}$, $Z_{\min}$ boundaries, zero-Neumann boundary conditions are applied due to symmetry. The relative permittivity of the sphere is set to 4. The floating potential of the sphere is calculated from the jump condition at the sphere surface. Particles are pre-loaded into the domain and absorbed/injected at all three ambient boundaries ($X_{\max}, Y_{\max}, Z_{\max}$) following stationary Maxwellian distributions and reflected at all three symmetric boundaries ($X_{\min}, Y_{\min}, Z_{\min}$). 216 macro-particles are used per PIC cell per species. The time step is set as $d\hat{t} = 0.005$.

The field solution approaches to the steady state at about $\hat{t} = 200$. The IFE-PIC solution of the floating potential is $\phi_s|_{IFE-PIC} \approx -2.3708$ at $\hat{t} = 220$ whereas $\phi_s|_{OML} \approx -2.3602$. The relative error of the floating potential for the last a few steps are about 3%. Fig. 7 compares IFE-PIC solution and analytic OML solution for the 1D potential profiles in the $r \geq R_s$

Table 4
Solar wind plasma and photoelectron (at 90° SEA) parameters.

Species	Number density n (cm^{-3})	Drifting velocity v_d (km/s)	Temperature T (eV)
s.w.e.	8.7	468	12
s.w.i.	8.7	468	10
photo.e.	64	N/A	2.2

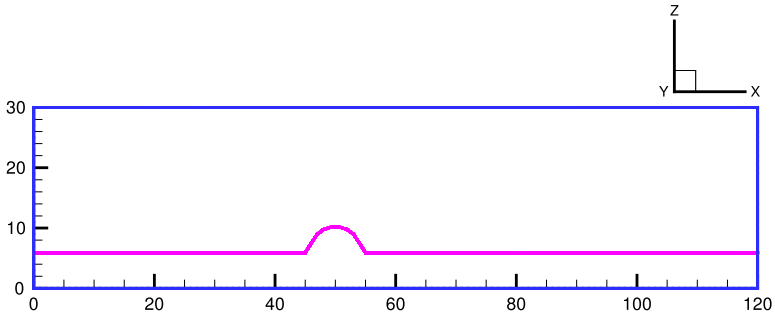

Fig. 8. Simulation domain and interface for the lunar plasma interactions.

region at $\hat{t} = 220$. The results show that the IFE-PIC solution agrees very well with the analytic solution from the revised OML theory [13,61].

5. Application to PIC simulations of plasma–surface interaction at the lunar terminator

In this section, we present simulations of plasma–surface interactions at the lunar terminator under an average solar wind condition. The interface is defined by an algebraic equation $z = z(x, y)$ such that the sub-domain above the interface is space and the sub-domain below is lunar regolith. In the following, we will discuss briefly the plasma conditions considered in those simulations, and the simulation setup of the plasma–surface interactions. Then we present the simulation results with brief discussions.

5.1. Plasma species

The plasma species considered in this example include solar wind ions, solar wind electrons, and photoelectrons. Here, we consider the average solar wind condition. The parameters of the plasma species are listed in Table 4, where "s.w.e." stands for "solar wind electrons", "s.w.i." for "solar wind ions", and "photo.e." for "photoelectrons". All the plasma species are normalized based on photoelectrons at 90° Sun Elevation Angle (SEA) condition [67].

5.2. Simulation setup

The simulation domain has a size of $120 \times 10 \times 30$ PIC cells with mesh size 1.38 m (the Debye length of photoelectrons at 90° SEA) in each dimension. For the illustration purpose, the local lunar surface terrain is modeled as a 3D cosine-curved column on a flat surface as described by the following equation:

$$\hat{z} = \hat{z}(\hat{x}, \hat{y}) = \begin{cases} 0.5 \cdot (-\cos\frac{\hat{x}-45}{10} + 1) \cdot 4.3 + 5.9, & (45 \le \hat{x} \le 55), \\ 5.9, & (\hat{x} < 45 \text{ or } \hat{x} > 55). \end{cases} \tag{5.44}$$

See Fig. 8 for an illustration of a 2D cut of the domain along the y-axis.

It is necessary to point out that the lunar surface is not a part of the boundary of the simulation domain but an interface (see Fig. 8). The medium below the interface has the physical meaning of the surface regolith of the Moon. In this setup, the regolith thickness is set to be 5.9×1.38 m which is a typical value for most areas on the lunar surface [54,60]. The relative permittivity of the lunar surface regolith is set to 4 [29,67]. The summit of the local lunar surface is of height 4.3×1.38 m.

Dirichlet field boundary conditions are applied at $Z_{\max}$ (top) boundary which represents the far-field plasma condition. Zero-Neumann boundary conditions are applied at all other five boundaries. Particles representing solar wind electrons and ions are pre-loaded into the simulation domain and absorbed/injected at the boundaries $X_{\min}$ (left), $X_{\max}$ (right), and $Z_{\max}$ (top) following their respective Maxwellian distributions. 64 macro-particles are used per PIC cell per species for solar wind plasma. For photoelectrons, macro-particles are generated together with local sunlit condition such that about 4 macro-particles are generated per time step under normal incidence. Reflection particle boundary conditions are applied in the y-direction. Photoelectrons are emitted from the sunlit regions at each PIC step and leave positive charges on the lunar surface. Particles hitting the surface are collected and charges carried by the particles are deposited at the surface for the calculation of surface charging. In the cases presented here, the solar wind flows at an incidence angle of 5° in the

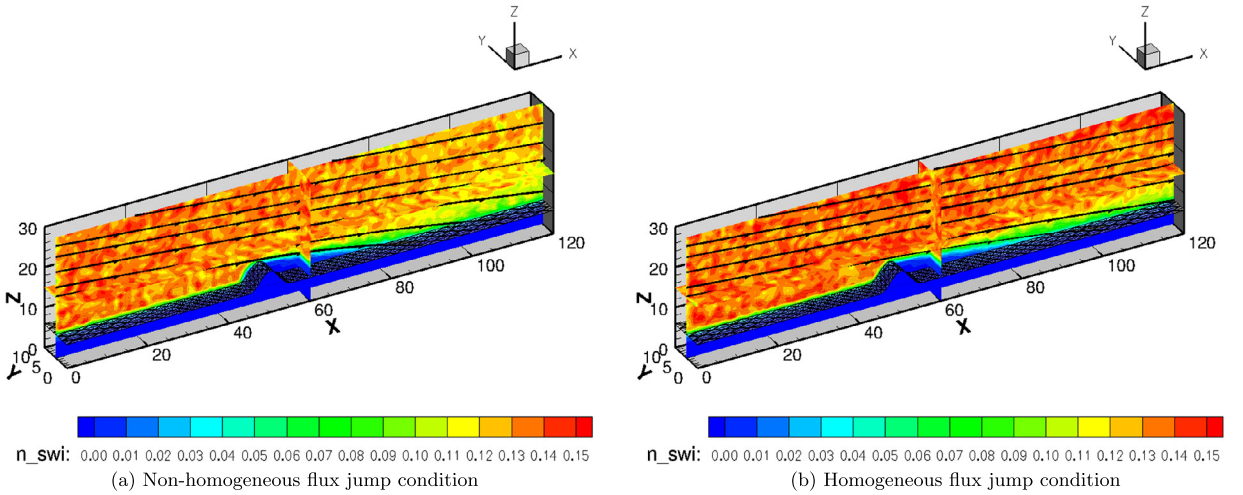

(a) Non-homogeneous flux jump condition (b) Homogeneous flux jump condition

Fig. 9. Density contours of solar wind ions. Normalized by 64 cm^{-3}.

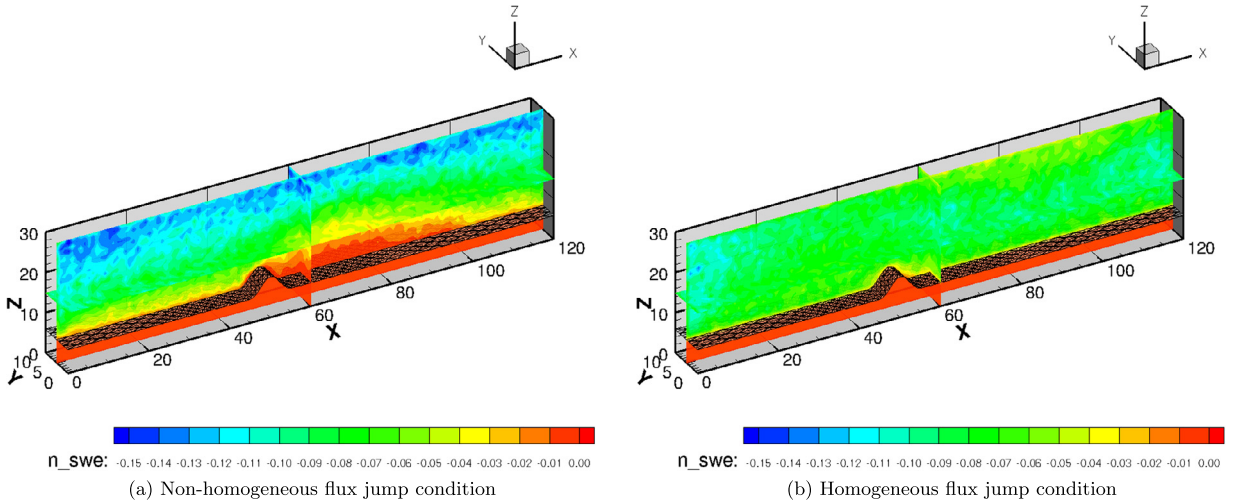

(a) Non-homogeneous flux jump condition (b) Homogeneous flux jump condition

Fig. 10. Density contours of solar wind electrons. Normalized by 64 cm^{-3}.

$X-Z$ plane towards the lunar surface and the solar illumination angle is assumed to be the same as the solar wind flowing direction. The time step is set to be $d\hat{t} = 0.1$.

5.3. Results and discussions

To illustrate the effects of the non-homogeneous flux jump condition on the solution of lunar surface charging, we present simulation results using both the non-homogeneous flux jump condition algorithm and the homogeneous flux jump condition algorithm. The results shown are taken at $\hat{t} = 600$. Figs. 9 through 11 compare the steady state density contours of solar wind ions (with streamlines), solar wind electrons, and photoelectrons, respectively. The solar wind ion density contour plots clearly show that a plasma wake [65] is created by the local uneven surface. While the ion density contours generated by both models are similar, the solar wind electron density contour (Fig. 10) and photoelectron density contour plots (Fig. 11) show significant differences between the two models. For instance, the non-homogeneous flux jump condition algorithm resolves the sheath structure in the solar wind electron density contours and the non-uniform spatial distribution of the photoelectrons, which are the features missed from the plots generated by the homogeneous flux jump condition algorithm. The features shown in the Figs. 10 and 11 reflect the effects of the surface electric field. (Such effects are not obvious in the ion density contour plot, Fig. 9, because the kinetic energy of the stream ions are orders of magnitude larger than that of the electric field energy and hence, the perturbation of the surface potential on ion dynamics is insignificant in this case.) The electric potential contours are compared in Fig. 12. The two algorithms lead to two totally different potential solutions. The non-homogeneous flux jump condition algorithm resolves the differential charging on the lunar surface and inside the regolith layer due to charge deposition from the plasma and/or photoelectron emission. The solution shows

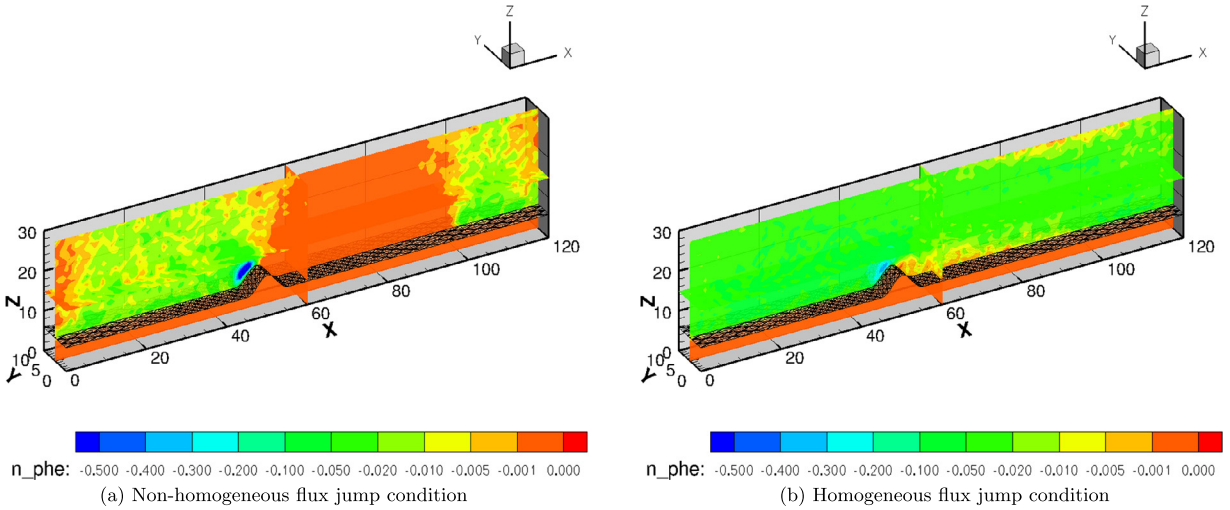

(a) Non-homogeneous flux jump condition (b) Homogeneous flux jump condition

Fig. 11. Density contours of photoelectrons. Normalized by 64 cm^{-3}.

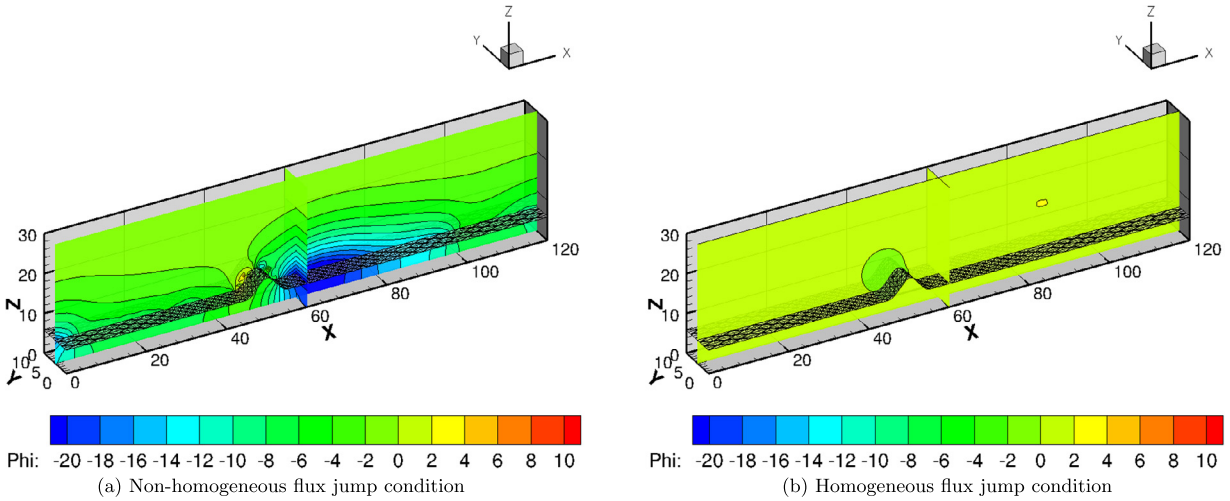

(a) Non-homogeneous flux jump condition (b) Homogeneous flux jump condition

Fig. 12. Potential contours. Normalized by 2.2 V.

that the surface potential is slightly positive in the sunlit/ram region due to photoelectron emission and negative in the wake region due to lack of ions in the wake [65]. On the other hand, the differential charging is not resolved under the homogeneous flux condition algorithm because the effect of charge deposition on surface is not included. This leads to an incorrect solution to the electric field.

Such plasma environments and electric fields indicate complex interactions between plasma environments and the lunar surface, which further influence the transport of charged dust grains under the localized electric field. Therefore, the self-consistent resolution of lunar surface potential along with the plasma environment will provide more accurate knowledge about the plasma environment for future exploration missions. This numerical example validates our new IFE-PIC simulation tool and demonstrates its capability to handle a variety of complicated and realistic space plasma environments (solar wind plasma, photoelectrons, etc.) interacting with bodies of non-trivial geometries (lunar surface, asteroidal surfaces, etc.).

6. Conclusions

In this paper, we constructed a new 3D IFE space and utilized it in a Galerkin formulation to solve the 3D second order elliptic partial differential equations with discontinuous coefficient and non-homogeneous flux jump conditions, which has an important application in the PIC simulations of the plasma environment on the lunar surface. The mesh of the IFE method can be independent of the interface location. Our numerical experiments demonstrate that the new IFE space has the optimal approximation capability and the IFE method with Galerkin formulation has the optimal convergence rates. We also improved the PIC method and combined it with the new IFE method in order to form the new IFE-PIC method with non-homogeneous flux jump conditions, which is utilized to simulate the plasma environment at the lunar terminator.

References

[1] S. Adjerid, M. Ben-Romdhane, T. Lin, Higher degree immersed finite element methods for second-order elliptic interface problems, Int. J. Numer. Anal. Model. 11 (3) (2014) 541–566.
[2] S. Adjerid, T. Lin, p-th degree immersed finite element for boundary value problems with discontinuous coefficients, Appl. Numer. Math. 59 (6) (2009) 1303–1321.
[3] I. Babuška, The finite element method for elliptic equations with discontinuous coefficients, Computing 5 (1970) 207–213.
[4] C.K. Birdsall, A.B. Langdon, Plasma Physics via Computer Simulation, Taylor & Francis Group, New York, 2005.
[5] J.H. Bramble, J.T. King, A finite element method for interface problems in domains with smooth boundary and interfaces, Adv. Comput. Math. 6 (1996) 109–138.
[6] B. Camp, T. Lin, Y. Lin, W. Sun, Quadratic immersed finite element spaces and their approximation capabilities, Adv. Comput. Math. 24 (1–4) (2006) 81–112.
[7] Y. Cao, Y. Chu, X.-M. He, T. Lin, An iterative immersed finite element method for an electric potential interface problem based on given surface electric quantity, J. Comput. Phys. 281 (2015) 82–95.
[8] Z. Chen, J. Zou, Finite element methods and their convergence for elliptic and parabolic interface problems, Numer. Math. 79 (1998) 175–202.
[9] S. Chou, An immersed linear finite element method with interface flux capturing recovery, Discrete Contin. Dyn. Syst., Ser. B 17 (7) (2012) 2343–2357.
[10] S. Chou, D.Y. Kwak, K.T. Wee, Optimal convergence analysis of an immersed interface finite element method, Adv. Comput. Math. 33 (2) (2010) 149–168.
[11] Y. Chu, Y. Cao, X.-M. He, M. Luo, Asymptotic boundary conditions for two-dimensional electrostatic field problems with immersed finite elements, Comput. Phys. Commun. 182 (11) (2011) 2331–2338.
[12] D.M. Cook, The Theory of the Electromagnetic Field, Prentice-Hall, Englewood Cliffs, 1975.
[13] Gian Luca Delzanno, Xian-Zhu Tang, Comparison of dust charging between orbital-motion-limited theory and particle-in-cell simulations, Phys. Plasmas 22 (November 2015) 113703.
[14] D. Depew, D. Han, J. Wang, X.-M. He, T. Lin, Immersed-finite-element particle-in-cell simulations of lunar surface charging, #199, in: Proceedings of the 13th Spacecraft Charging Technology Conference, Pasadena, California, June 23–27, 2014.
[15] R.E. Ewing, Z. Li, T. Lin, Y. Lin, The immersed finite volume element methods for the elliptic interface problems, Modelling '98 (Prague), Math. Comput. Simul. 50 (1–4) (1999) 63–76.
[16] W.M. Farrell, T.J. Stubbs, J.S. Halekas, R.M. Killen, G.T. Delory, M.R. Collier, R.R. Vondrak, Anticipated electrical environment within permanently shadowed lunar craters, J. Geophys. Res. 115 (2010) E03004.
[17] W. Feng, X.-M. He, Y. Lin, X. Zhang, Immersed finite element method for interface problems with algebraic multigrid solver, Commun. Comput. Phys. 15 (4) (2014) 1045–1067.
[18] Y. Gong, B. Li, Z. Li, Immersed-interface finite-element methods for elliptic interface problems with non-homogeneous jump conditions, SIAM J. Numer. Anal. 46 (2008) 472–495.
[19] Y. Gong, Z. Li, Immersed interface finite element methods for elasticity interface problems with non-homogeneous jump conditions, Numer. Math., Theory Methods Appl. 3 (1) (2010) 23–39.
[20] X.-M. He, Bilinear immersed finite elements for interface problems, PhD dissertation, Virginia Polytechnic Institute and State University, 2009.
[21] X.-M. He, T. Lin, Y. Lin, Approximation capability of a bilinear immersed finite element space, Numer. Methods Partial Differ. Equ. 24 (5) (2008) 1265–1300.
[22] X.-M. He, T. Lin, Y. Lin, A bilinear immersed finite volume element method for the diffusion equation with discontinuous coefficients, Commun. Comput. Phys. 6 (1) (2009) 185–202.
[23] X.-M. He, T. Lin, Y. Lin, Interior penalty discontinuous Galerkin methods with bilinear IFE for a second order elliptic equation with discontinuous coefficient, dedicated to Professor David Russell's 70th birthday, J. Syst. Sci. Complex. 23 (3) (2010) 467–483.
[24] X.-M. He, T. Lin, Y. Lin, Immersed finite element methods for elliptic interface problems with non-homogeneous jump conditions, Int. J. Numer. Anal. Model. 8 (2) (2011) 284–301.
[25] X.-M. He, T. Lin, Y. Lin, The convergence of the bilinear and linear immersed finite element solutions to interface problems, Numer. Methods Partial Differ. Equ. 28 (1) (2012) 312–330.
[26] X.-M. He, T. Lin, Y. Lin, A selective immersed discontinuous Galerkin method for elliptic interface problems, Math. Methods Appl. Sci. 37 (7) (2014) 983–1002.
[27] X.-M. He, T. Lin, Y. Lin, X. Zhang, Immersed finite element methods for parabolic equations with moving interface, Numer. Methods Partial Differ. Equ. 29 (2) (2013) 619–646.
[28] B. Heinrich, Finite Difference Methods on Irregular Networks, International Series of Numerical Mathematics, vol. 82, Birkhäuser, Boston, 1987.
[29] W.D. Carrier III, G.R. Olhoeft, W. Mendell, Lunar Sourcebook: A User's Guide to the Moon, Cambridge University Press, 1991, pp. 475–594.
[30] J.D. Jackson, Classical Electrodynamics, third edition, Wiley, New York, 1999.
[31] H. Ji, J. Chen, Z. Li, A symmetric and consistent immersed finite element method for interface problems, J. Sci. Comput. 61 (3) (2014) 533–557.
[32] H. Jian, Y. Chu, H. Cao, Y. Cao, X.-M. He, G. Xia, Three-dimensional IFE-PIC numerical simulation of background pressure's effect on accelerator grid impingement current for ion optics, Vacuum 116 (2015) 130–138.
[33] R. Kafafy, Immersed finite element particle-in-cell simulations of ion propulsion, PhD dissertation, Virginia Polytechnic Institute and State University, 2005.
[34] R. Kafafy, T. Lin, Y. Lin, J. Wang, Three-dimensional immersed finite element methods for electric field simulation in composite materials, Int. J. Numer. Methods Eng. 64 (7) (2005) 940–972.
[35] R. Kafafy, J. Wang, Whole subscale ion optics simulation: direct ion impingement and electron backstreaming, in: 41st AIAA/ASME/SAE/ASEE Joint Propulsion Conference and Exhibit, AIAA 2005-3691, Tucson, Arizona, July 2005.
[36] R. Kafafy, J. Wang, Whole ion optics gridlet simulations using a hybrid-grid immersed-finite-element particle-in-cell code, J. Propuls. Power 23 (1) (January–February 2007) 59–68.
[37] R. Kafafy, J. Wang, T. Lin, A hybrid-grid immersed-finite-element particle-in-cell simulation model of ion optics plasma dynamics, Dyn. Contin. Discrete Impuls. Syst., Ser. B, Appl. Algorithms 12 (2005) 1–16.
[38] D.Y. Kwak, K.T. Wee, K.S. Chang, An analysis of a broken p_1-nonconforming finite element method for interface problems, SIAM J. Numer. Anal. 48 (6) (2010) 2117–2134.
[39] T. Lee, Y. Chang, J. Choi, D. Kim, W. Liu, Y. Kim, Immersed finite element method for rigid body motions in the incompressible Navier–Stokes flow, Comput. Methods Appl. Mech. Eng. 197 (25–28) (2008) 2305–2316.
[40] Z. Li, The immersed interface method using a finite element formulation, Appl. Numer. Math. 27 (3) (1997) 253–267.
[41] Z. Li, K. Ito, The Immersed Interface Method: Numerical Solutions of PDEs Involving Interfaces and Irregular Domains, Frontiers in Applied Mathematics, vol. 33, Society for Industrial and Applied Mathematics (SIAM), Philadelphia, PA, 2006.
[42] Z. Li, T. Lin, Y. Lin, R.C. Rogers, An immersed finite element space and its approximation capability, Numer. Methods Partial Differ. Equ. 20 (3) (2004) 338–367.

[43] Z. Li, T. Lin, X. Wu, New Cartesian grid methods for interface problems using the finite element formulation, Numer. Math. 96 (1) (2003) 61–98.
[44] Z. Li, X. Yang, An immersed finite element method for elasticity equations with interfaces. Recent advances in adaptive computation, Contemp. Math. 383 (2005) 285–298.
[45] T. Lin, Y. Lin, W. Sun, Error estimation of a class of quadratic immersed finite element methods for elliptic interface problems, Discrete Contin. Dyn. Syst., Ser. B 7 (4) (2007) 807–823.
[46] T. Lin, Y. Lin, W. Sun, Z. Wang, Immersed finite element methods for 4th order differential equations, J. Comput. Appl. Math. 235 (13) (2011) 3953–3964.
[47] T. Lin, Y. Lin, X. Zhang, Immersed finite element method of lines for moving interface problems with nonhomogeneous flux jump, Contemp. Math. 586 (2013) 257–265.
[48] T. Lin, Y. Lin, X. Zhang, Partially penalized immersed finite element methods for elliptic interface problems, SIAM J. Numer. Anal. 53 (2) (2015) 1121–1144.
[49] T. Lin, D. Sheen, The immersed finite element method for parabolic problems with the Laplace transformation in time discretization, Int. J. Numer. Anal. Model. 10 (2) (2013) 298–313.
[50] T. Lin, D. Sheen, X. Zhang, A locking-free immersed finite element method for planar elasticity interface problems, J. Comput. Phys. 247 (2013) 228–247.
[51] T. Lin, J. Wang, An immersed finite element electric field solver for ion optics modeling, in: Proceedings of AIAA Joint Propulsion Conference, Indianapolis, IN, July, 2002, AIAA, 2002-4263.
[52] T. Lin, J. Wang, The immersed finite element method for plasma particle simulation, in: Proceedings of AIAA Aerospace Sciences Meeting, Reno, NV, Jan., 2003, AIAA, 2003-0842.
[53] T. Lin, X. Zhang, Linear and bilinear immersed finite elements for planar elasticity interface problems, J. Comput. Appl. Math. 236 (18) (2012) 4681–4699.
[54] D.S. McKay, G. Heiken, A. Basu, G. Blanford, S. Simon, R. Reedy, B.M. French, J. Papike, The lunar regolith, in: Lunar Sourcebook: a User's Guide to the Moon, Cambridge University Press, 1991, pp. 285–356, chapter 7.
[55] A. Poppe, M. Horányi, Simulations of the photoelectron sheath and dust levitation on the lunar surface, J. Geophys. Res. 115 (2010) A08106.
[56] A.R. Poppe, Modeling, theoretical and observational studies of the lunar photoelectron sheath, PhD thesis, University of Colorado, Boulder, 2011.
[57] A.R. Poppe, M. Piquette, A. Likhanskii, M. Horányi, The effect of surface topography on the lunar photoelectron sheath and electrostatic dust transport, Icarus 221 (2012) 135–146.
[58] T. Preusser, M. Rumpf, S. Sauter, L.O. Schwen, 3D composite finite elements for elliptic boundary value problems with discontinuous coefficients, SIAM J. Sci. Comput. 33 (5) (2011) 2115–2143.
[59] A.A. Samarskiĭ, V.B. Andreev, Méthods aux Différences pour Équations Ellipticques, Mir, Moscow, 1978.
[60] Y.G. Shkuratov, N.V. Bondarenko, Regolith layer thickness mapping of the moon by radar and optical data, Icarus 149 (2) (February 2001) 329–338.
[61] Xian-Zhu Tang, Gian Luca Delzanno, Orbital-motion-limited theory of dust charging and plasma response, Phys. Plasmas 21 (December 2014) 123708.
[62] Vahid Vahedi, G. DiPeso, Simultaneous potential and circuit solution for two-dimensional bounded plasma simulation codes, J. Comput. Phys. 131 (1) (February 1997) 149–163.
[63] S. Vallaghè, T. Papadopoulo, A trilinear immersed finite element method for solving the electroencephalography forward problem, SIAM J. Sci. Comput. 32 (4) (2010) 2379–2394.
[64] J. Wang, Y. Cao, R. Kafafy, J. Pierru, V. Decyk, Ion propulsion simulations using parallel supercomputers, in: 29th International Electric Propulsion Conference, Princeton, NJ, Oct. 31–Nov.4, 2005, IEPC, 2005-271.
[65] J. Wang, D.E. Hastings, Ionospheric plasma flow over large high-voltage space platforms. II: the formation and structure of plasma wake, Phys. Fluids, B Plasma Phys. 4 (6) (June 1992) 1615–1629.
[66] J. Wang, X.-M. He, Y. Cao, Modeling spacecraft charging and charged dust particle interactions on lunar surface, in: Proceedings of the 10th Spacecraft Charging Technology Conference, Biarritz, France, 2007.
[67] J. Wang, X.-M. He, Y. Cao, Modeling electrostatic levitation of dusts on lunar surface, IEEE Trans. Plasma Sci. 36 (5) (2008) 2459–2466.
[68] P. Wang, Immersed finite element particle-in-cell modeling of surface charging in rarefied plasmas, PhD dissertation, Virginia Polytechnic Institute and State University, 2010.
[69] H. Xie, Z. Li, Z. Qiao, A finite element method for elasticity interface problems with locally modified triangulations, Int. J. Numer. Anal. Model. 8 (2) (2011) 189–200.
[70] X. Zhang, Nonconforming immersed finite element methods for interface problems, PhD dissertation, Virginia Polytechnic Institute and State University, 2013.